Sensors & Actuators: B. Chemical 390 (2023) 133913

Contents lists available at ScienceDirect

Sensors and Actuators: B. Chemical

journal homepage: www.elsevier.com/locate/snb

Integrated sensor for humidity, temperature, light, and carbon dioxide based on passive RFID

Fengjuan Miao [a,*,1], Yue Han [a,1], Pengbo Tian [a], Bairui Tao [a,*], Yu Zang [b], Paul K. Chu [c]

[a] College of Communications and Electronics Engineering, Qiqihar University, Heilongjiang 161006, China
[b] College of Materials Science and Engineering, Qiqihar University, Wenhua street 42, Qiqihar, China
[c] Department of Physics, Department of Materials Sciences and Engineering, and Department of Biomedical Engineering, City University of Hong Kong, Tat Chee Avenue, Kowloon, Hong Kong, China

ARTICLE INFO

Keywords:
Radio frequency identification
Passive sensor
Humidity-temperature-light-carbon dioxide sensor
Low cost

ABSTRACT

In recent years, radio frequency identification (RFID) technology has been widely used in smart agriculture. In order to measure the multi-dimensional environmental information during the planting of agricultural products, this paper proposes an integrated humid temperature phosgene (HTLC) sensor based on passive RFID. The structure is optimized by the HFSS software and the multi-dimensional integrated sensor is prepared by engraving. The passive RFID HTLC multidimensional sensor operates stably at 10–50 %RH, 5–25 ℃, 700–1900 lux and 800–1600 ppm. The frequency shift is 80 MHz at 10–50 %RH and the sensitivity is 2 MHz/%RH. In the temperature range of 5–25 ℃, the amplitude change is 12.58 dB and the sensitivity is 0.63 dB/℃. For 700–1900 lux light, the amplitude variation is 10.03 dB and the sensitivity is 0.02 dB/Lux at room temperature. For CO2 concentrations of 800–1600 ppm, the sensor has an amplitude change of 9.43 dB and a sensitivity of 0.012 dB/ppm. The sensor has the advantages of low cost, fast response, good repeatability and good stability, and can collect and display the parameter information of the crop growth environment in multiple dimensions, making the monitoring and management more accurate and intelligent, and helping to adjust the growth environment of the crop in time, thereby improving the yield of the crop.

1. Introduction

Traditional agricultural production can no longer meet the demand by the modern society and smart agriculture has emerged [1,2]. Traditional radio frequency identification (RFID) tags consisting of antennas and integrated circuits (ICs) are quite expensive and passive chipless RFID tags have recently been proposed as a more economical alternative to barcodes [3,4]. RFID not only enables quick and accurate monitoring of environmental parameters in agriculture and cultivation, but also reduces the sensor cost. Some intelligent functions including perception of physical parameters and collection of environmental information have been introduced to chipless RFID [5–7] and chipless RFID sensors can be used for various identification and sensing purposes such as temperature [8,9], humidity [10,11], health [12], gas detection [13,14], positioning [15], strain [16], pipeline integrity [17], pressure [18], and metal defect detection [19,20].

In agricultural processes such as planting, it is necessary to control and monitor factors such as temperature, humidity, light intensity and CO_2 concentration in the crop environment and multi-functional sensors can bring the cost down [21]. Temperature and humidity chipless RFID sensors [22] have been proposed by considering the dielectric constant of the materials (affected by these two quantities) as well as expansion (only affected by temperature) and measurements achieved in controlled and real-world environments have demonstrated the potential. For example, a temperature-humidity-pressure (THP) sensor [23] composed of surface acoustic wave (SAW) devices can simultaneously monitor the temperature, humidity, and pressure. An LC wireless passive TPH sensor composed of low-temperature co-fired ceramics (LTCC) has been proposed by adopting the LC wireless passive technology [24] and it delivers stable performance in a wide range of TPH and harsh environments, but lacks the measurement of light and CO_2 in agricultural applications.

In summary, existing sensors can only measure two or three parameters and have limited data acquisition. In this paper, a high-quality,

* Corresponding authors.
E-mail addresses: miaofengjuan@163.com (F. Miao), tbr_sir@163.com (B. Tao).
[1] These are co-first authors.

https://doi.org/10.1016/j.snb.2023.133913
Received 14 February 2023; Received in revised form 28 April 2023; Accepted 1 May 2023
Available online 2 May 2023

low-cost passive RFID multi-dimensional integrated sensor was prepared and tested by hydrothermal method and RF simulation software HFSS by combining nanomaterials with RFID antennas. Multidimensional integrated sensors are prepared by engraving on a copper clad laminate as a substrate. This technology is simple and cost-effective, which can collect and display the parameter information of crop growth environment in multiple dimensions, making monitoring and management more accurate and intelligent, and helping to adjust the growing environment of crops in time, so as to improve crop yields.

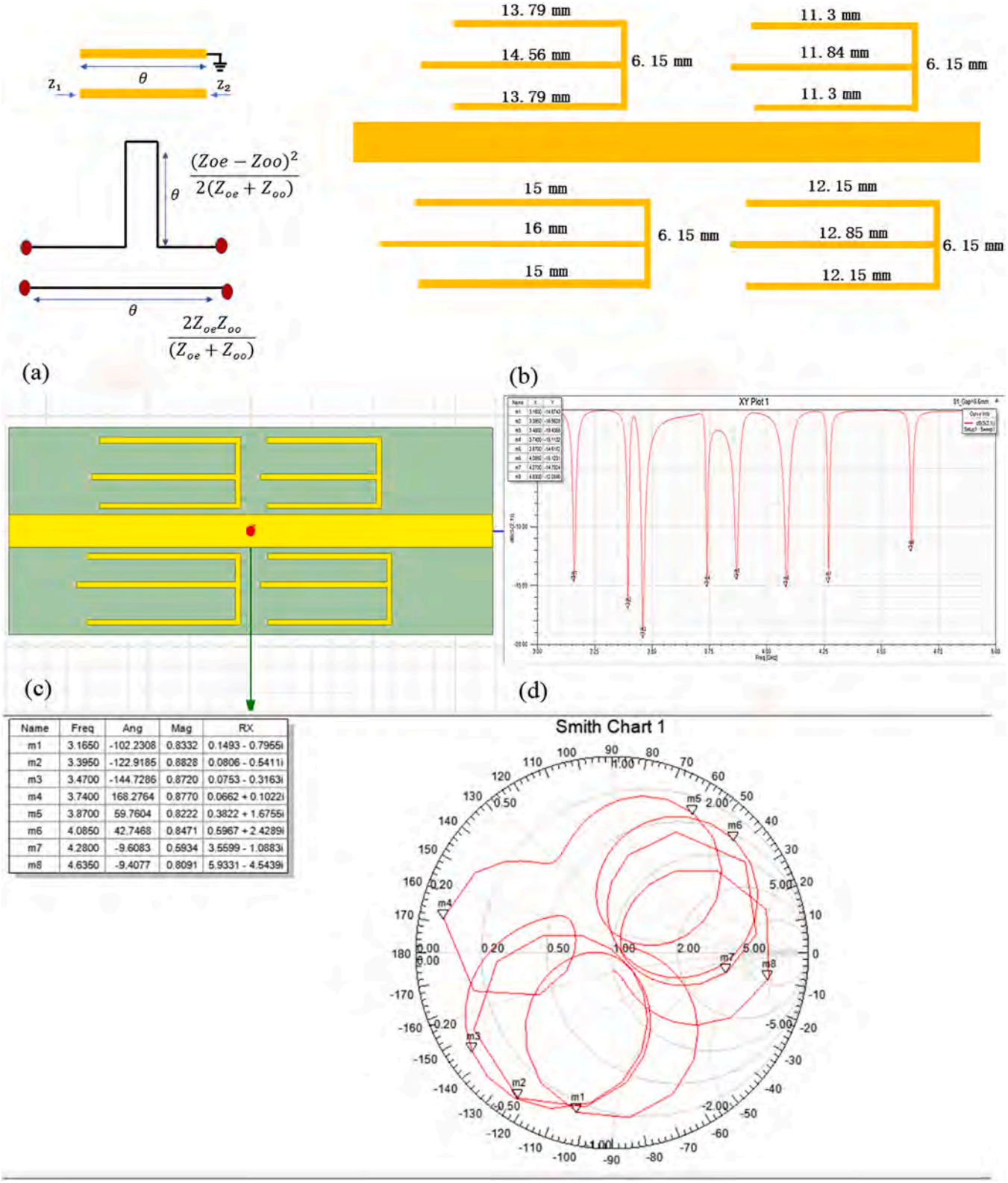

Name	Freq	Ang	Mag	RX
m1	3.1650	-102.2308	0.8332	0.1493 - 0.7955i
m2	3.3950	-122.9185	0.8828	0.0806 - 0.5411i
m3	3.4700	-144.7286	0.8720	0.0753 - 0.3163i
m4	3.7400	168.2764	0.8770	0.0662 + 0.1022i
m5	3.8700	59.7604	0.8222	0.3822 + 1.6755i
m6	4.0850	42.7468	0.8471	0.5967 + 2.4289i
m7	4.2800	-9.6083	0.5934	3.5599 - 1.0883i
m8	4.6350	-9.4077	0.8091	5.9331 - 4.5439i

Fig. 1. (a) Equivalent circuit of the sensor and (b) HFSS simulation model for the humidity sensor; (c) and (d) HFSS simulation results; (e) Smith circle diagram of a passive RFID sensing antenna.

2. Sensor structure

The sensing antenna is designed by generating a fixed frequency using a recently reported multi-state coupled resonator. The stopband characteristics of the resonator can be explained by the image impedances Z_1 and Z_2 [25,26]. As shown in Fig. 1(a), the image impedance of the coupling lines at ports 1 and 2 is:

$$Z_1 = \frac{2Z_{oe}Z_{oo}\cos\theta}{\sqrt{-(Z_{oe}-Z_{oo})^2+(Z_{oe}+Z_{oo})^2\cos^2\theta}} \quad (1)$$

$$Z_2 = \frac{Z_{oe}Z_{oo}}{Z_1} \quad (2)$$

where θ is the electrical length of the coupling line and Z_{oe} and Z_{oo} are the characteristic impedances of the even-mode and odd-mode, respectively. The equations show that fundamental stop band resonance occurs when the fundamental resonance frequency is $\theta = \pi/2$, that is, when the coupling line length is equal to 1/4 wavelength. This structure also exhibits stopband characteristics at all odd harmonics.

Fig. 1(b) shows the resonator after changing the length of the arms when all the arms are connected. The coupling segment length of the resonator is shown in Fig. 1(b). In this design, the copper clad laminate (length * width * thickness: 47 mm * 18 mm * 0.5 mm; Roughness: 0.4–0.6) is specified as a good substrate on which the multi-state coupled resonator is constructed as a multidimensional sensing antenna. By coating the nanocomposite as the HTLC sensitive materials on the arm of the resonator, the relevant parameters of the surrounding environment can be gauged by the degree of adsorption of the sensitive materials to the HTLC parameters in the environment, which in turn causes changes in the relative permittivity of the sensitive materials. H, X, and Y represent the thickness, width, and length of the multidimensional sensing antenna, respectively, as shown in Fig. 1(b). When the arm of the multidimensional sensor resonates, the scanning source is connected to a vector network analyzer with a certain frequency range and the relevant parameters of the multidimensional sensor circuit are detected to perform passive measurements of multiple parameters.

3. Simulation and preparation

3.1. Multidimensional antenna simulation

According to the resonance characteristics of the multi-state coupling resonator structure, the HFSS software is adopted to perform electromagnetic modeling and simulation, and analysis after setting the frequency sweep and other operations. As shown in Fig. 1(c), when the microstrip couples withg the line resonator cross-polarization incident wave, that is, excitation from one end of the microstrip line, the microstrip coupling line resonator absorbs most of the energy of the incident wave at some specific frequencies producing a resonant state. The insertion loss curve in the cross-polarization direction appears as a clear resonance wave valley at this resonance frequency and at other frequencies, most of the incident wave is reflected by the antenna. Fig. 1 (d) shows the simulation results of the multi-state coupled resonator and the band resistance characteristics are good. The resonator shows a total of 8 frequency points at 3.16 GHz, 3.39 GHz, 3.46 GHz, 3.74 GHz, 3.87 GHz, 4.08 GHz, 4.27 GHz, and 4.63 GHz, and the corresponding return loss S21 parameters are −14.6 dB, −16.9 dB, −19.4 dB, −15.11 dB, −14.5 dB, −15.12 dB, −14.7 dB, −12.06 dB, respectively. All resonators in this structure are connected to represent code 11 of each resonator and the configuration code is 111111111111 which can meet actual needs. The resonance characteristics of the microstrip coupling line resonator is analyzed by simulating the original drawing. As shown in Fig. 1(e), the impedance output of the Smith circle diagram of the microstrip antenna at the corresponding frequency meets the requirements of 50 Ω matched impedance and the power reflection of the terminal feeder is small for good impedance matching. At the same time, the performance of the antenna can be analyzed by the electromagnetic field and as shown in Fig. 2, the magnetic and electric fields are obtained by the HFSS simulation software. By observing the electric field distribution, it can be seen that the electric field intensity is large in the middle of the microstrip line and the magnetic field distribution map indicates that the energy is mainly concentrated at the resonator that provides the inductance. According to the magnetic field distribution, it is mainly concentrated in the structure that provides inductance and the electric field with high strength is mainly concentrated in the middle of the capacitor structure. When the microstrip coupling line resonator is excited by an electromagnetic wave horizontal to the surface along the microstrip direction, the capacitive structure and surrounding electric field couple because the resonator on both sides of the microstrip line has a highly symmetrical structure, so that magnetic coupling is weak. The electrical coupling energy performance is stronger and the capacitance of the antenna is larger than the capacitance of the same size proportion. The resonance frequency naturally becomes smaller, so as to achieve miniaturization and good resonance characteristics. Based on these results, 3.16 GHz, 3.46 GHz, 4.08 GHz, and 4.27 GHz are chosen as the frequency points of the passive RFID multidimensional sensor.

3.2. Antenna preparation

A machine was used to precisely engraving the single-parameter RFID sensing antenna. The substrate of the RFID sensing antenna was the FR-4 copper clad laminate and a PCB CNC engraving machine (Xuegu XG-1690A) was used. The advantage of the engraving machine is that the engraved pattern is relatively complete in spite of certain limitations. The model of the multi-state coupling resonator was exported by AutoCAD and the picture was imported into the carving butler software. The positioning test was carried out first to ensure the safety of engraving and that the milling cutter did not exceed the area required for engraving. After a series of debugging processes, the pattern was engraved.

3.3. Preparation of sensitive materials

Compared with other microelectronic processing methods, the humidity sensor is prepared by thermal transfer technology, which has the advantages of simple operation, high flexibility and low cost. Copper clad laminates with lower resistance were used as inductors and interconnect electrical insulation. The preparation of nano ZnO, nano MoS_2, nano TiO_2, nano Co_3O_4, nano In_2O_3, nano CuO, and RGO solution is illustrated in Fig. 3.

The pure SnO_2 powder was prepared by one-step hydrothermal method. Tin chloride was the raw materials for synthesis of tin oxide and zinc acetate was used to adjust the pH of the solution to modify the morphology of tin oxide. 15 ml of absolute ethanol and 15 ml of deionized water were mixed and 0.7 g of tin chloride and 0.6 g of sodium hydroxide were dissolved. Zinc acetate (0.05 g) was added to adjust the pH and the solution was sonicated magnetically to produce a milky white liquid. The solution was added to a high-temperature reactor and heated to 180 ℃ for 24 h. After the hydrothermal reaction was complete, the reactor cooled to room temperature and the product was rinsed with a large amount of absolute ethanol and deionized water. The product was dried at 60 ℃ for 12 h to obtain a white tin oxide powder. The synthesis steps are shown in Fig. 3(a).

The pure MoS_2 powder was prepared by a one-step hydrothermal method. A mixture of 0.038 mol $(NH_4)\ 6Mo_7O_{24}{\cdot}4\ H_2O$ and 0.065 mol CH_4N_2S was added to 40 ml of deionized water and mixed ultrasonically for 10 min. The solution was placed in an autoclave lined with Teflon and heated to 180 ℃ for 12 h. After cooling to room temperature, the black pellet was washed with deionized water and dried at 60 ℃ for 30 min. The synthesis steps are shown in Fig. 3(b).

The pure ZnO powder was prepared by a one-step hydrothermal

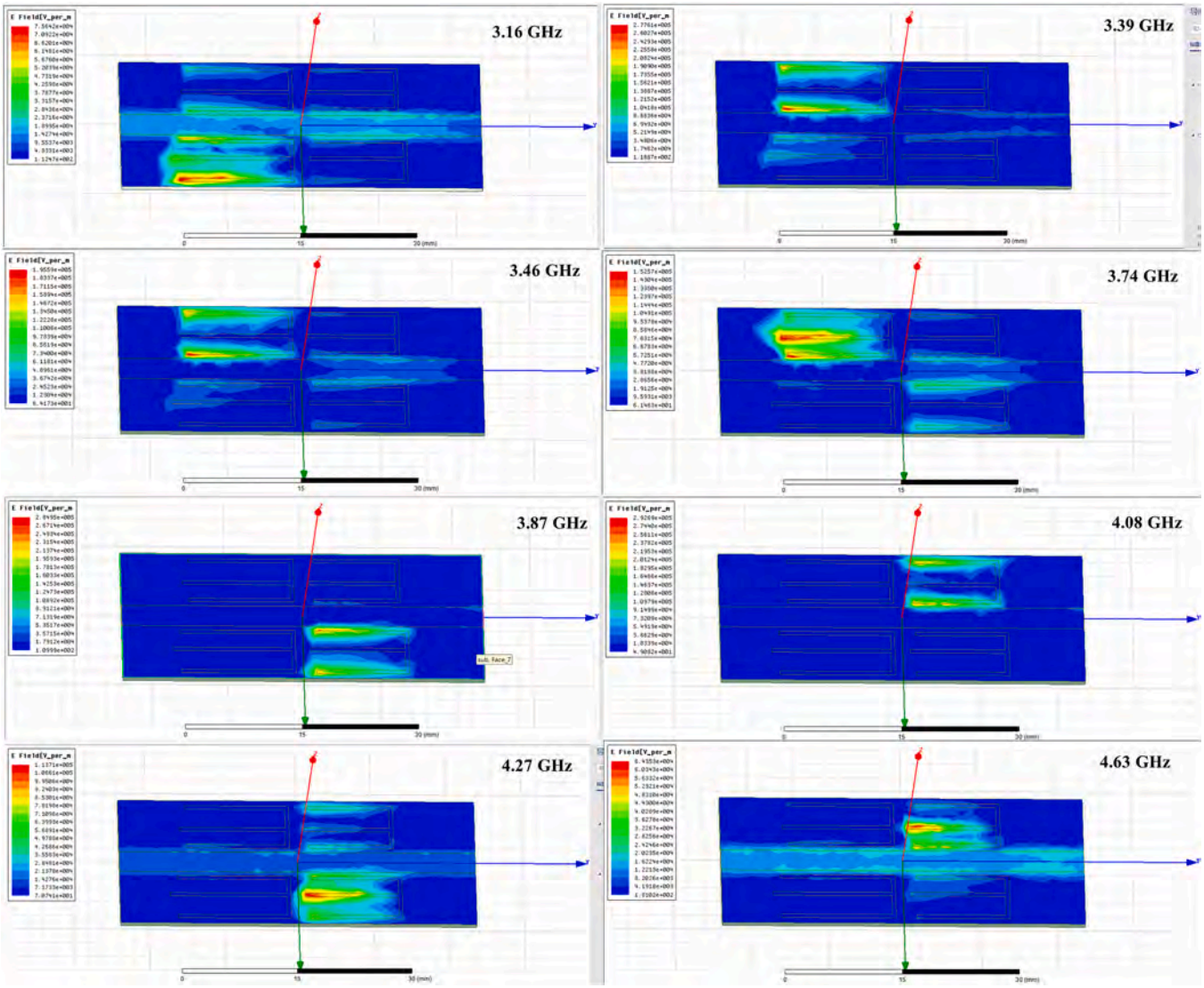

Fig. 2. Electromagnetic field distribution at a single frequency.

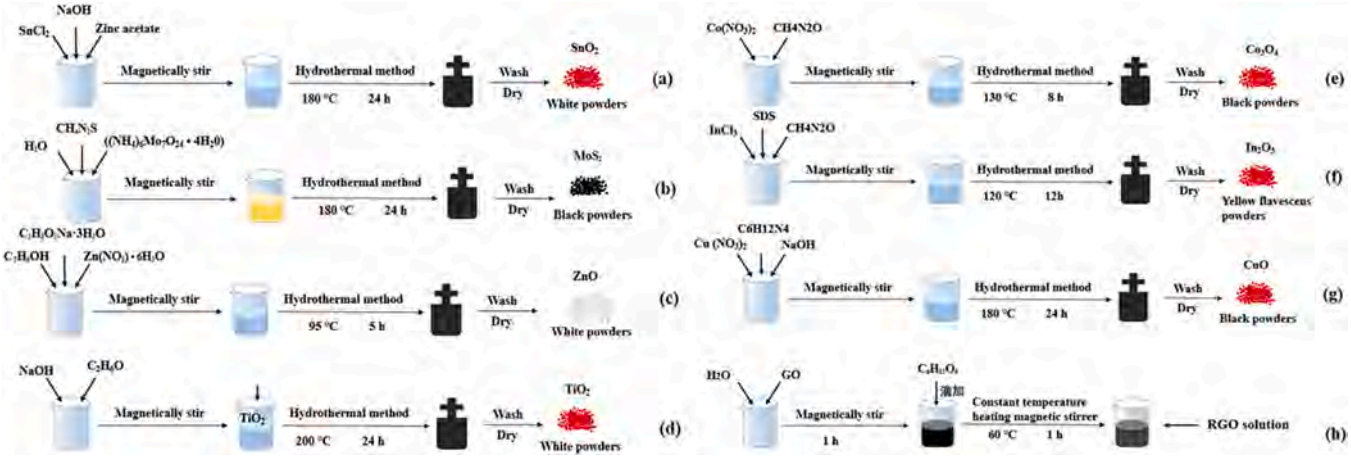

Fig. 3. Preparation of nano-sensitive materials by the hydrothermal method.

method. 0.05 mmol $ZnNO_3{\cdot}6H_2O$ and 1 mmol HMTA were mixed with 50 ml of deionized water and sonicated for 10 min. It was placed in a Teflon-lined autoclave and heated to 95 ℃ for 5 h. After cooling to room temperature, the white pellet was rinsed with deionized water and dried at 60 ℃ for 30 min. The synthesis steps are shown in Fig. 3(c).

The pure TiO_2 powder was prepared by a one-step hydrothermal

method. 40 g of the sodium hydroxide aqueous solution and 20 ml of absolute ethanol were mixed with a 1:1 vol ratio and 1 g of titanium dioxide granular powder was added and sonicated to produce a homogeneous solution. The solution was placed in a 50 ml high-temperature reactor at 200 ℃ for 24 h. After cooling, sampling, and filtering, it was rinsed with deionized water and diluted hydrochloric acid several times and dried at 60 ℃ for 12 h after the pH was adjusted to 7 to obtain the nano-linear titanium dioxide powder. The synthesis steps are shown in Fig. 3(d).

The pure Co_3O_4 powder was prepared by a one-step hydrothermal method. 1.5 mmol $Co(NO_3)_2$ and 7.5 mmol urea were dissolved in 50 ml of deionized water to a homogeneous solution under vigorous agitation for 5 min. The solution was placed in a 50 ml Teflon-lined stainless-steel autoclave containing a piece of nickel foam, sealed, and heated to 130 ℃ for 8 h. After natural cooling to room temperature, the product was removed, rinsed several times with deionized water, dried at 60 ℃ for 30 min, annealed at 300 ℃ for 2 h, and cooled naturally to room temperature. The synthesis steps are shown in Fig. 3(e).

The pure In_2O_3 powder was prepared by a one-step hydrothermal method. Indium chloride was dissolved in deionized water and a certain amount of $C_{12}H_{25}SO_4Na$(SDS) and urea was added and stirred magnetically for 30 min to form a white suspension. It was put into a high-pressure reactor and treated at a hydrothermal temperature of 120 ℃ for 12 h. After the reaction, the upper liquid was drained before the precipitate was collected by centrifugation with deionized water and absolute ethanol. The white sediment was place on a glass dish and dried at 60 ℃ for 24 h. In_2O_3 was obtained by placing the dried sample in a muffle furnace and annealing at 500 ℃ for 2 h. The synthesis steps are shown in Fig. 3(f).

The pure CuO powder was prepared by a one-step hydrothermal method. 10 ml of the 1 mol/L copper nitrate solution was mixed with 10 ml of 1.00 mol/L sodium hydroxide and 2 g of methylenetetramine powder were added and stirred. Keeping the substrate the same, the solution was divided into three parts. 15 ml of ethanol, ethylene glycol, and distilled aqueous solution were added to the three parts, stirred for 15 min to obtain a homogeneous solution, placed in a high-pressure reactor of PTFE, and heated to 120 ℃ for 12 h. The solution was then removed, centrifuged with distilled water three times, washed three times with absolute ethanol, and dried in a 50 ℃ oven to finally obtain the CuO black powder. The synthesis steps are shown in Fig. 3(g).

The graphene oxide (GO) powder was purchased from Nanjing XFNANO Material Technology Co., Ltd. It was monolayer graphene oxide powder with a diameter of 0.5–5 μm and thickness of 0.8–1.2 nm. Analytical grade glucose was purchased from Tianjin Kemeiou Chemical Reagent Co., Ltd. 50 mg of GO were put in 10 ml of deionized water, sonicated for 60 min to obtain a GO dispersion, diluted with 40 ml of absolute ethanol, and sonicated to obtain 50 ml of the GO dispersion with a concentration of 1 mg/ml. 0.3 mol glucose powder was added to 5 ml of deionized water and sonicated for 5 min to obtain the glucose solution. It was stirred magnetically and heated in a water bath to 60 ℃ for 60 min while the glucose solution was dripped in between. After cooling to room temperature, a reduced graphene oxide (RGO) solution is obtained. The synthesis steps are shown in Fig. 3(h).

4. Results and discussion

4.1. Characterization

The SEM diagram of the SnO_2/MoS_2/RGO mixture at low magnification is shown in Fig. 4(a), and the morphological characteristics of the SnO_2/MoS_2/RGO mixture and the nanostructure of each can be observed. It can be clearly distinguished that the surrounding globules are SnO_2, the flowers are MoS_2, and the flake material surrounded in the middle is a graphene nanosheet.The transmission electron microscopy

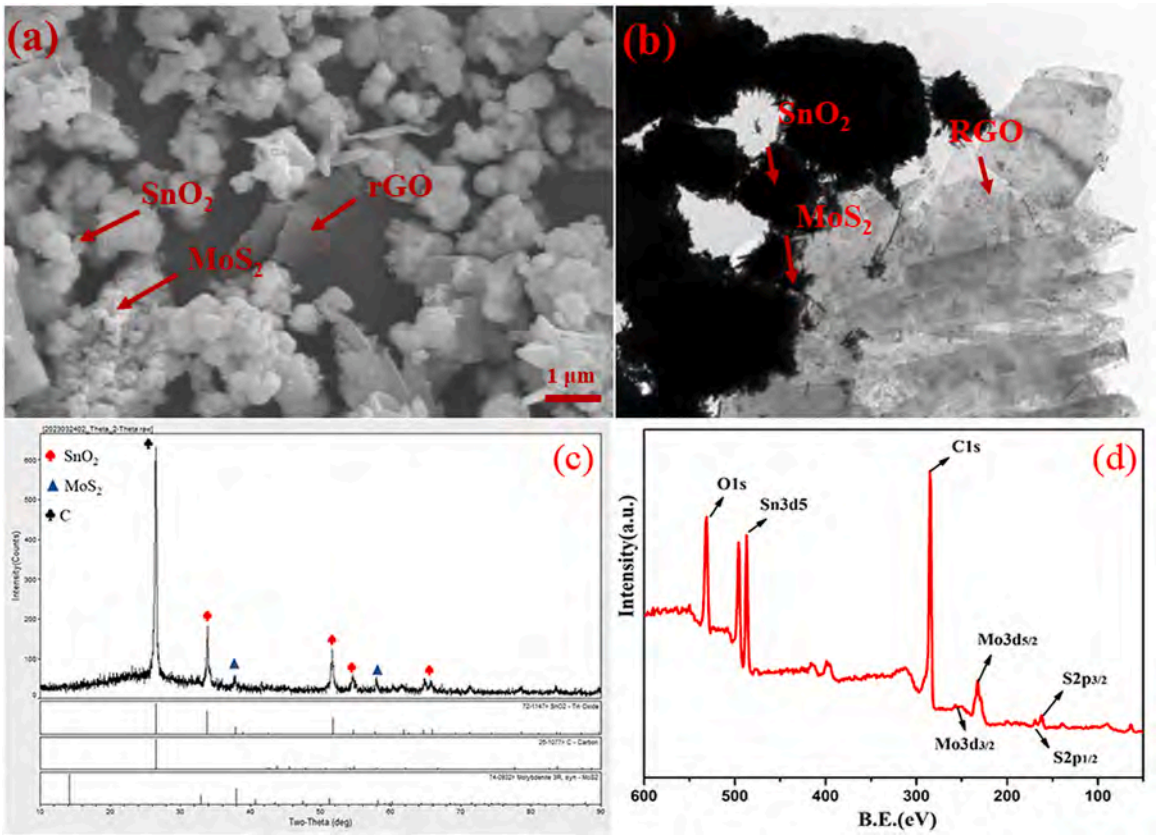

Fig. 4. (a) is the SEM characterization of SnO_2/MoS_2/RGO, (b) is the TEM characterization of SnO_2/MoS_2/RGO; (c) is the XRD diagram of SnO_2/MoS_2/RGO, and (d) is the XPS diagram of SnO_2/MoS_2/RGO.

diagram of SnO_2/MoS_2/RGO mixture under the aggregation of more substances is shown in Fig. 4(b), the flake black matter is RGO, MoS_2 is flower-like, and SnO_2 is nanospherical, because of agglomeration, nanospheres are grouped together. Transmission electron microscopy can only observe that the projected image does not reflect the stereomorphology, so nanoflowers and nanospheres appear as spots or agglomerates into large spheres. However, it can be clearly seen that the sheet RGO is covered with SnO_2/MoS_2 balls, which shows that SnO_2/MoS_2/RGO has been fully mixed, which is more conducive to moisture adsorption.The crystalline phase structure and composition of SnO_2/MoS_2/RGO nanocomposites were characterized by X-ray diffraction (XRD) (Fig. 4(c)). The diffraction values of SnO_2 (JCPDS No. 77-0449) at 2θ were 26.48°, 33.83°, 37.72°, 51.56° and 78.50°, respectively, and the diffraction values of MoS_2 (JCPDS No. 17-0744) at 2θ were 14.533°, 33.026°, 34.061°, 38.370°, respectively. 41.107°, 48.130°, 58.315°, 60.501°, and 76.154°, corresponding to crystal planes (003), (101), (012), (104), (015), (107), (110), (113) and (119). RGO (JCPDS No. 26–1080) has a diffraction value of 26.603° at 2θ, corresponding to a crystal plane of (004). X-ray photoelectron spectroscopy (XPS) composites are used to make photoelectron spectra to obtain the composition of the composites. The complete spectrum of the SnO_2/MoS_2/RGO nanocomposites shown in Fig. 4(d) shows the presence of the main Mo 3d, S2p, C1s, O1s, and Sn 3d peaks.

The microscopic morphology of nanomaterials was characterized by scanning electron microscopy (SEM), Fig. 5(a) is the micromorphology characterization map of ZnO/MoS_2/RGO nanocomposites, and the ZnO in Fig. 5 is clearly distinguished, which proves that the ZnO prepared in the hydrothermal process has an ideal morphology, and can clearly distinguish the thin flake-like RGO, and the nanoflower-like MoS_2 structure is loose and porous, with a larger specific surface area, and can better adsorb water molecules. This structure well reflects the excellent conductivity of RGO and the sensitive characteristics of ZnO modified by MoS_2. The micro-regions of ZnO/MoS_2/RGO nanocomposites were further studied by observing the ultrastructure inside the composite by transmission electron microscopy (TEM) (Fig. 5(b)). In the TEM diagram of Fig. 5(b), the different morphological characteristics of ZnO, MoS_2 and RGO can be clearly displayed, and in the ultramicro environment, we can see that RGO is a very thin nanosheet, while ZnO is the same as the SEM figure in the nanorod-like shape, and the nanoflower-like MoS2 is composed of thicker nanosheets than RGO. The crystalline phase structure and composition of ZnO/MoS_2/RGO nanocomposites were characterized by X-ray diffraction (XRD) (Fig. 5(c)). The diffraction values of ZnO (JCPDS No. 89-0511) at 2θ were 31.776°, 34.431°, 36.263°, 47.552°, 56.610°, 62.875° and 67.967°, respectively, corresponding to crystal planes of (100), (002), (101), (102), (110), (103) and (112). The crystal planes of MoS_2 and RGO are described above. X-ray photoelectron spectroscopy (XPS) composites are used to make photoelectron spectra to obtain the composition of the composites. The complete spectrum of the ZnO/MoS_2/RGO nanocomposites shown in Fig. 5(d) shows the presence of the main Mo3d, S2p, C1s, O1s, and Zn2P peaks.

SEM and TEM morphology characterization are shown in Fig. 6(a,b), respectively, by characterizing the morphological characteristics of the microscopic region of the sensitive electrode, it can be seen from the figure that the prepared TiO_2 is indeed nano-linear, compared with particles and sheets, nano-linear TiO_2 has better performance, but when combined with sheet RGO, it is too tight, so a layer of Co_3O_4 is added between the two to modify the sensitive material, and the nanospherical Co_3O_4 forms a three-dimensional structure between TiO_2 and RGO. Make the structure of the overall sensitive material more three-dimensional. The crystalline phase structure and composition of TiO_2/Co_3O_4/RGO nanocomposites were characterized by X-ray diffraction (XRD) (Fig. 6(c)). The diffraction peaks of TiO_2 at 2θ are at 27.45°, 36.09°, 39.19°, 41.23°, 44.05°, 54.32°, 56.64°, 62.74°, 64.04°,

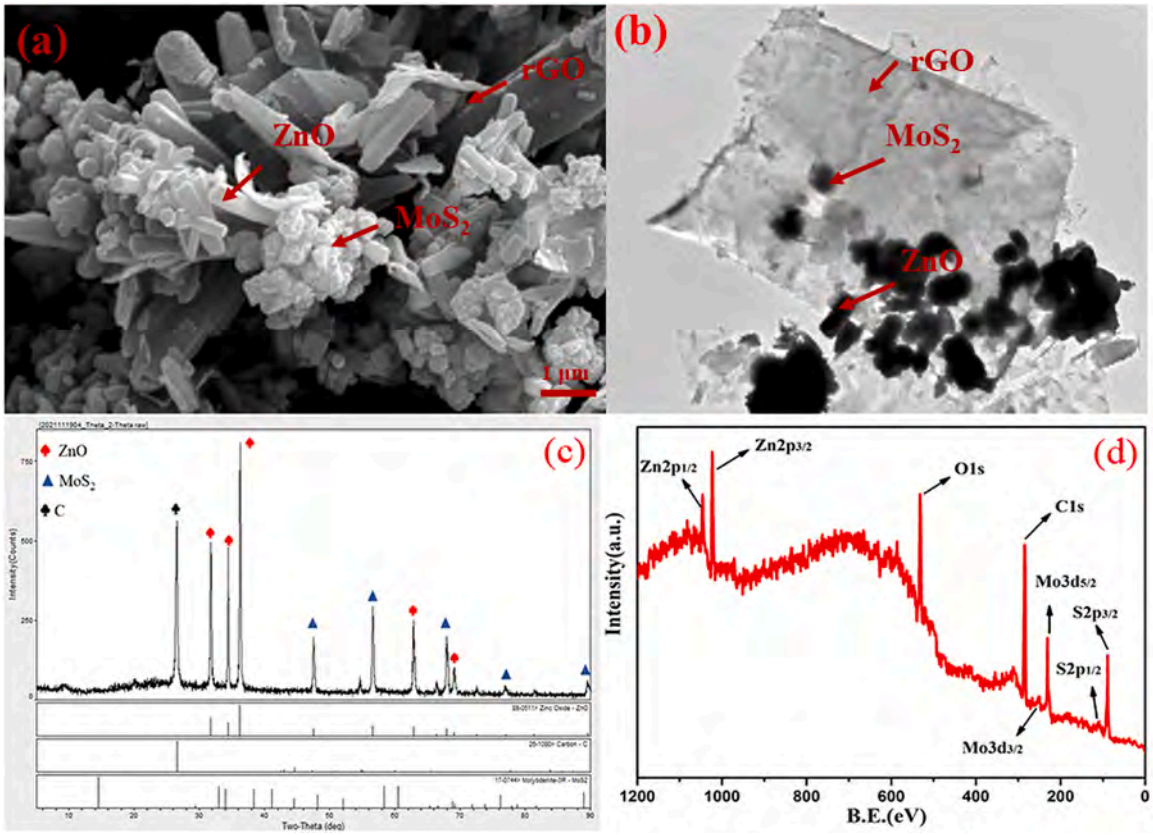

Fig. 5. (a) is the SEM characterization of ZnO/MoS_2/RGO, (b) is the TEM characterization of ZnO/MoS_2/RGO; (c) is the XRD diagram of ZnO/MoS_2/RGO, and (d) is the XPS diagram of ZnO/MoS_2/RGO.

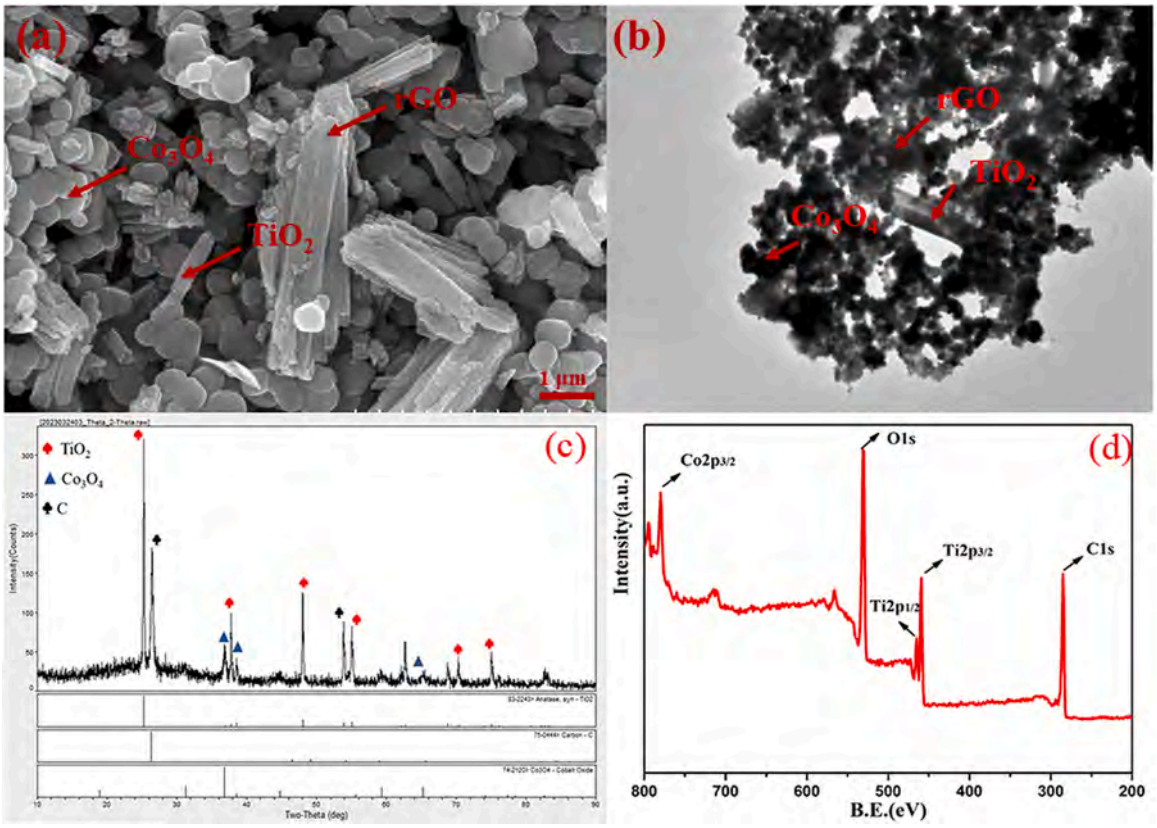

Fig. 6. (a) is the SEM characterization of TiO_2/Co_3O_4/RGO, (b) is the TEM characterization of TiO_2/Co_3O_4/RGO; (c) is the XRD diagram of TiO_2/Co_3O_4/RGO, and (d) is the XPS diagram of TiO_2/Co_3O_4/RGO.

69.01° and 69.79°, which correspond to (110), (101), (200), (111), (210), (211), (220), respectively of the quadripartite TiO_2 structure (JCPDS No. 21-1276), The diffraction values of (002), (310), (301) and (112), Co_3O_4 (JCPDS No. 42-1467) at 2θ are 19.000°, 31.271°, 36.852°, 44.808°, 59.357° and 65.236°, respectively, corresponding to crystal planes of (111), (220), (311), (400), (511) and (440). The complete spectrum of the TiO_2/Co_3O_4/RGO nanocomposites shown in Fig. 6(d) shows the presence of the main, Co2p, C1s, O1s, and Ti2P peaks.

The morphological characterization of SEM and TEM of sensitive materials is shown in Fig. 7(a,b), observing the morphological characteristics of the microscopic area of the sensitive electrode, it can be found that the prepared In_2O_3 is a nanoflower-like nanomaterial, after nanospherical CuO modification, and nano-sheet-like RGO combined with each other to form a larger specific surface area, when the oxygen molecules in the air seize a certain number of electrons from the conduction band, and then convert into different forms of oxygen ions resulting in a decrease in the number of electrons inside the material. Therefore, in the process of detecting CO_2, the electron transport after contact between CO_2 molecules in the environment and sensitive materials is more efficient, and the sensor performance is better. The crystalline phase structure and composition of In_2O_3/CuO/RGO nanocomposites were characterized by X-ray diffraction (XRD) (Fig. 7(c)). In_2O_3 (JCPDS No.06-0416) corresponds to crystal faces of (211), (222), (400), (411), (322), (431), (440) and (112) at 2θ, and the diffraction values of CuO (JCPDS No. 68-8601) at 2θ are 35.5°, 38.8°, 65.9° and 75.5°, respectively, and the corresponding crystal planes are (002), (200), (022) and (004). The complete spectrum of the In_2O_3/CuO/RGO nanocomposites shown in Fig. 7(d) shows the presence of major In 3d, Cu2p, C1s, and O1s peaks.

4.2. Sensing properties

After engraving, the sensing characteristics are determined as shown in Fig. 8. The JKZ1 sound tester is used to adjust the environmental parameters in the chamber. The measured and simulated S21 are compared and a very small movement is observed. The slight deviation between the simulation and experimental curves is mainly because the conductors and insulators in the simulation are considered to be ideal conductors but may be related to the manufacturing process and/or the parasitic capacitance introduced by the SMA connector. Since the sensitivity of the antenna sensor is expressed in the normalized frequency shifts $\Delta y/\Delta x$, deviations at the frequency do not have any impact on the performance of the antenna sensor. After testing, sensitive materials are applied to the antenna at the corresponding frequency points based on simulation results to measure the sensing parameters of humidity, temperature, Light, and CO_2. To simplify observation, only a plot of four frequency points is shown here.

As shown in Fig. 9(a), the S21-f of the HTLC sensor is evaluated in the indoor environment and one of them is measured while keeping the indoor environmental parameters unchanged. When humidity increases from 10 %RH to 50 %RH and increases by 10 %RH every 5 min, a frequency point representing a change in humidity of 80 MHz indicates a sensitivity of 2 MHz/%RH. Due to the adsorption of water by nanomaterials, temperature-sensitive materials, photosensitive materials and gas-sensitive materials exhibit slight dielectric constant changes, which in turn affect the temperature, illuminance and CO_2 in the curve. The frequency points vary by 25 MHz, 15 MHz, and 18 MHz, respectively, and are negligible due to the small variation. The resulting data are linearly fitted, as shown in Fig. 9(b), linearity $R^2 = 0.99749$. Repeatability performance was explored by repeating a process similar to the response and recovery process three times, and the experimental results are shown in Fig. 9(c). Experiments show that SnO_2/MoS_2/RGO

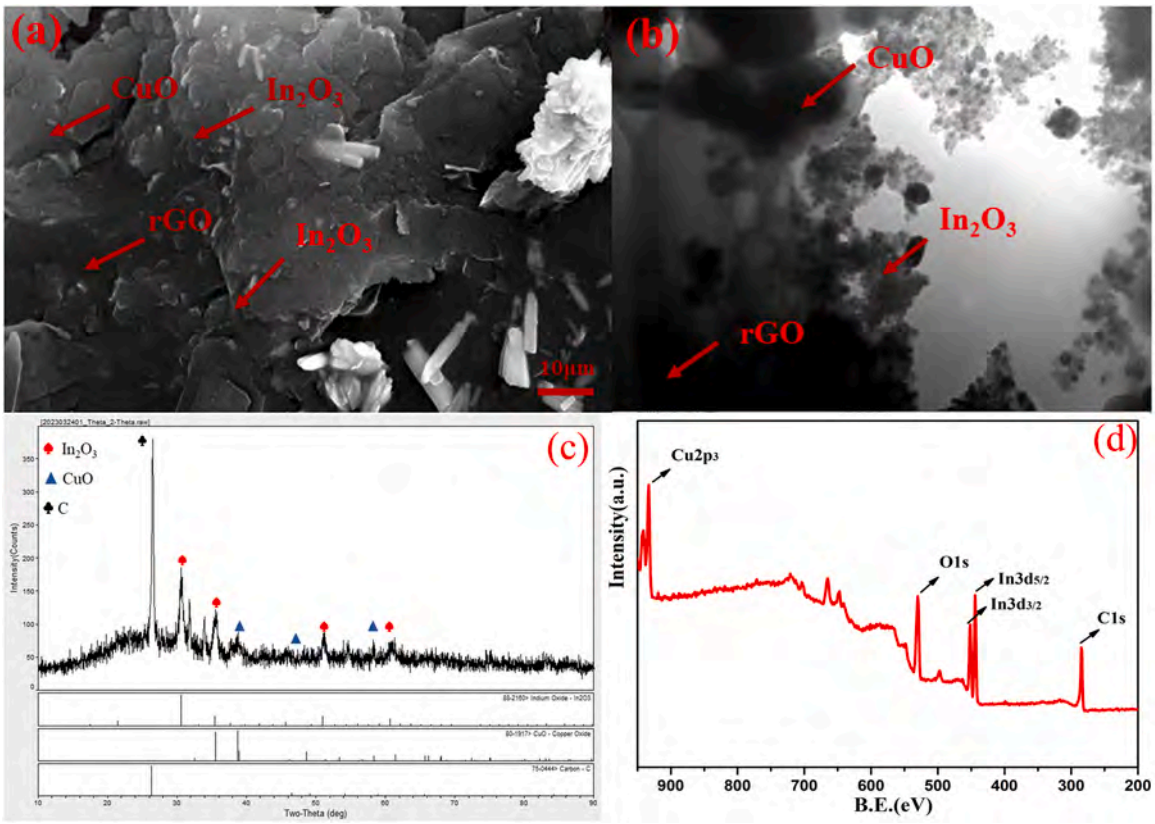

Fig. 7. (a) is the SEM characterization of In_2O_3/CuO/RGO, (b) is the TEM characterization of In_2O_3/CuO/RGO; (c) is the XRD diagram of In_2O_3/CuO/RGO, and (d) is the XPS diagram of In_2O_3/CuO/RGO.

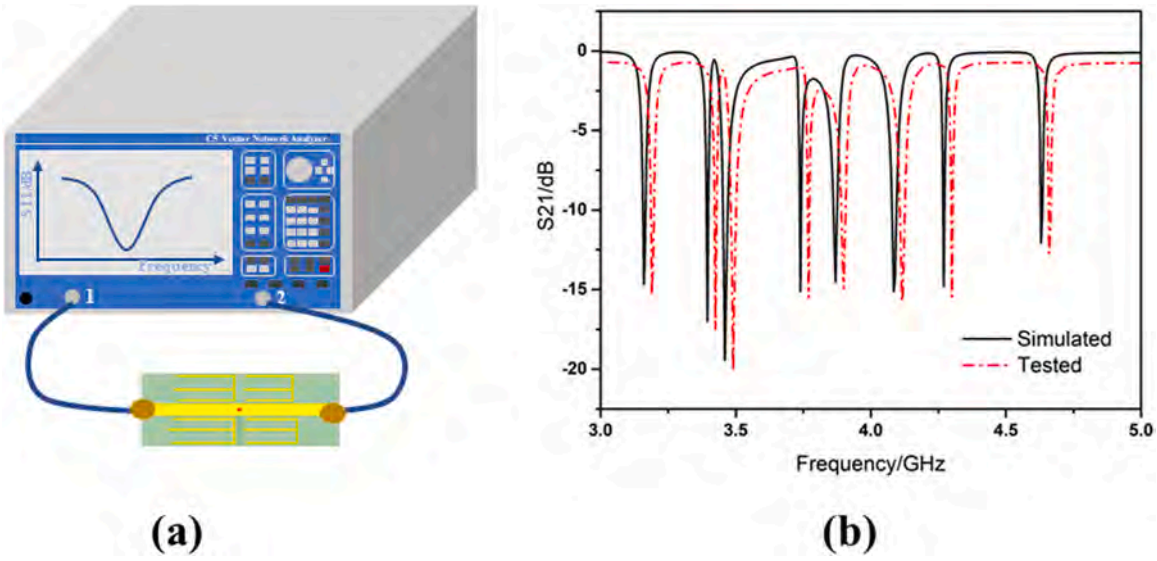

Fig. 8. (a) Environmental test and (b) Simulation and testing results.

composites have good repeatability in three cycles and can be used as repeatable sensing materials for humidity detection. Finally, the necessary stability of the applicable sensor was studied for 1 h under 10 %RH, 20 %RH, 30 %RH, 40 %RH, 50 %RH conditions, and the results are shown in Fig. 9(d). The results show that the prepared humidity sensor has good stability under low humidity and high humidity, so as to simulate the stable moisture sensitive properties of SnO_2/MoS_2/RGO in humid environment.

Fig. 10(a) shows that when the temperature increases from 5 ℃ to 25 ℃ every 3 min by 5 ℃, the frequency point representing the temperature changes slightly, but the amplitude changes by 12.58 dB and the sensitivity is 0.63 dB/℃. Since the material used to prepare the sensing antenna is a copper clad laminate, the curves representing humidity, illuminance, and CO_2 vary with temperature, and the amplitude changes by 5.02 dB, 4.35 dB, and 3.7 dB, respectively. The resulting data are linearly fitted, as shown in Fig. 10(b), linearity $R^2 = 0.81949$. Repeatability performance was explored by repeating a process similar to the response and recovery process three times, and the experimental

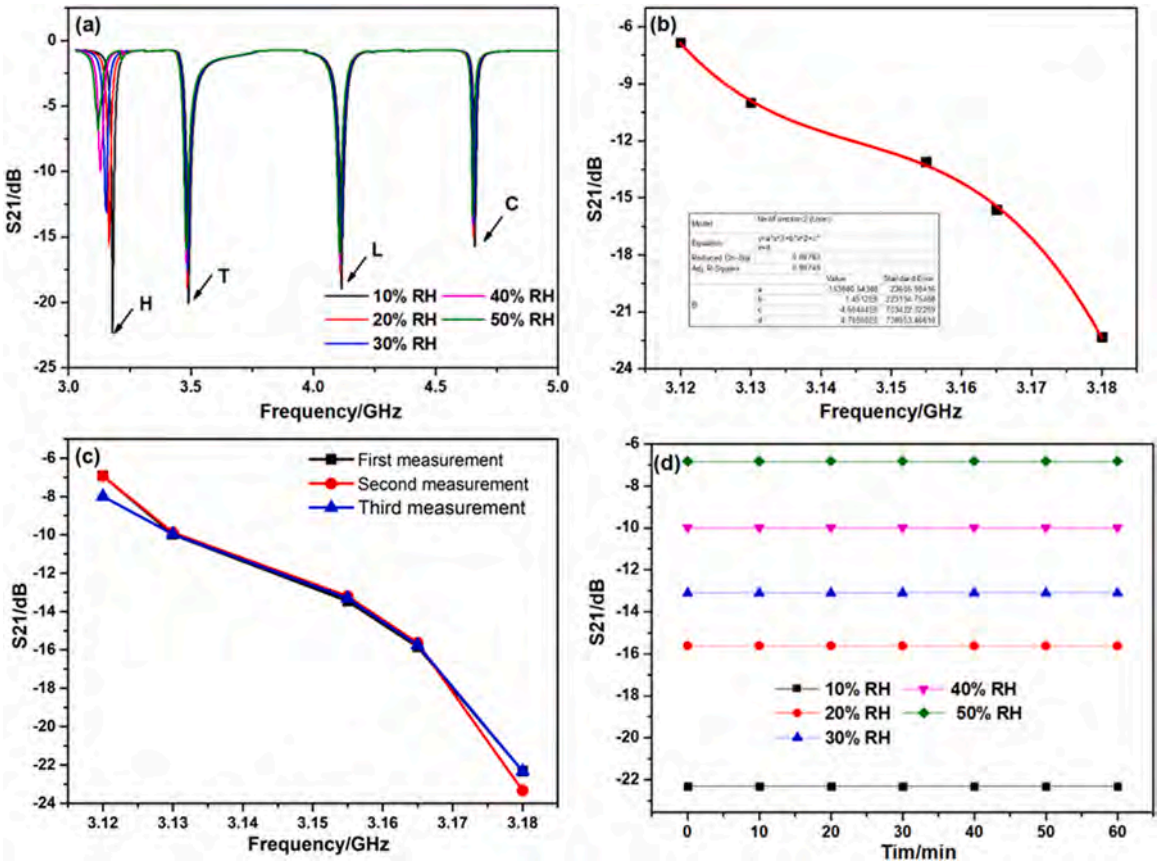

Fig. 9. (a) Effect of different humidity on sensor f; (b) Humidity sensor f response diagram; (c) repeatability testing; (d) stability testing.

results are shown in Fig. 10(c). Experiments show that ZnO/MoS_2/RGO composites have good repeatability in three cycles and can be used as repeatable sensing materials for humidity detection. Finally, the necessary stability of the applicable sensor was studied for 1 h at 5 ℃, 10 ℃, 15 ℃, 20 ℃, 25 ℃, and the results are shown in Fig. 10(d). The results show that the prepared humidity sensor has good stability under low humidity and high humidity, so as to simulate the stable temperature sensitive properties of ZnO/MoS_2/RGO in humid environment.

As shown in Fig. 11(a), when the light intensity increases from 700 Lux to 1300 Lux every 3 min by 300 Lux, a small change in the frequency representing illumination with an amplitude of 10.03 dB and a sensitivity of 0.02 dB/Lux can be observed. At the same time, with the increase of light intensity, the curves indicating humidity, temperature and CO_2 changed, and the amplitude changed by 1.58 dB, 3.24 dB and 1.02 dB, respectively. The resulting data are linearly fitted, as shown in Fig. 11(b), linearity $R^2 = 0.62828$. Reproducibility performance was explored by repeating a process similar to the response and recovery process three times, and the experimental results are shown in Fig. 11 (c). Experiments show that TiO_2/Co_3O_4/RGO composites have good repeatability in three cycles and can be used as repeatable sensing materials for humidity detection. Finally, the necessary stability of the applicable sensor was studied for 1 h at 700 Lux, 1000 Lux, 1300 Lux, 1600 Lux, 1900 Lux, and the results are shown in Fig. 11(d). The results show that the prepared humidity sensor has good stability under low humidity and high humidity, which simulates the stable photosensitive properties of TiO_2/Co_3O_4/RGO in humid environment.

Fig. 12(a) represents a slight change in frequency of CO_2 concentration with an amplitude change of 9.43 dB and a sensitivity change of 0.012 dB/ppm. At the same time, with the increase of CO_2 concentration, the curves indicating humidity, temperature and light intensity changed by 1.34 dB, 2.25 dB and 0.98 dB, respectively. The resulting data are linearly fitted, as shown in Fig. 12(b), linearity $R^2 = 0.62828$. Reproducibility performance was explored by repeating a process similar to the response and recovery process three times, and the experimental results are shown in Fig. 12(c). Experiments show that In_2O_3/CuO/RGO composites have good repeatability in three cycles and can be used as repeatable sensing materials for humidity detection. Finally, the necessary stability of the applicable sensor was studied for 1 h at 800 ppm, 1000 ppm, 1200 ppm, 1400 ppm, 1600 ppm, and the results are shown in Fig. 12(d). The results show that the prepared humidity sensor has good stability under low humidity and high humidity, and simulates the stable gas-sensitive properties of In_2O_3/CuO/RGO in humid environment.

4.3. Reaction mechanism

As shown in Fig. 13(a), the resistance of temperature-sensitive materials changes correspondingly with the change of outdoor ambient temperature, and when the ambient temperature rises, the volume of ZnO may expand slightly, which will lead to the deformation of the polarity therein, resulting in a strong electric field transferring the charge from the original structure to the new structure, reducing the insulation performance of the circuit, and the resistance of the temperature-sensitive material gradually increases or decreases, causing the antenna parameters to change.

As shown in Fig. 13(b), the characteristics of humidity-sensitive materials are related to the size of the dielectric constant, and the larger the value of the dielectric constant, the more polarization energy is required when the temperature-sensitive material is polarized, and when the ambient temperature of the temperature-sensitive material gradually increases, the internal molecular activity of the material gradually increases, and the polarization energy increases accordingly, resulting in a corresponding change in the volume of ZnO nanorods, and the relative permittivity will gradually increase. Changes in the

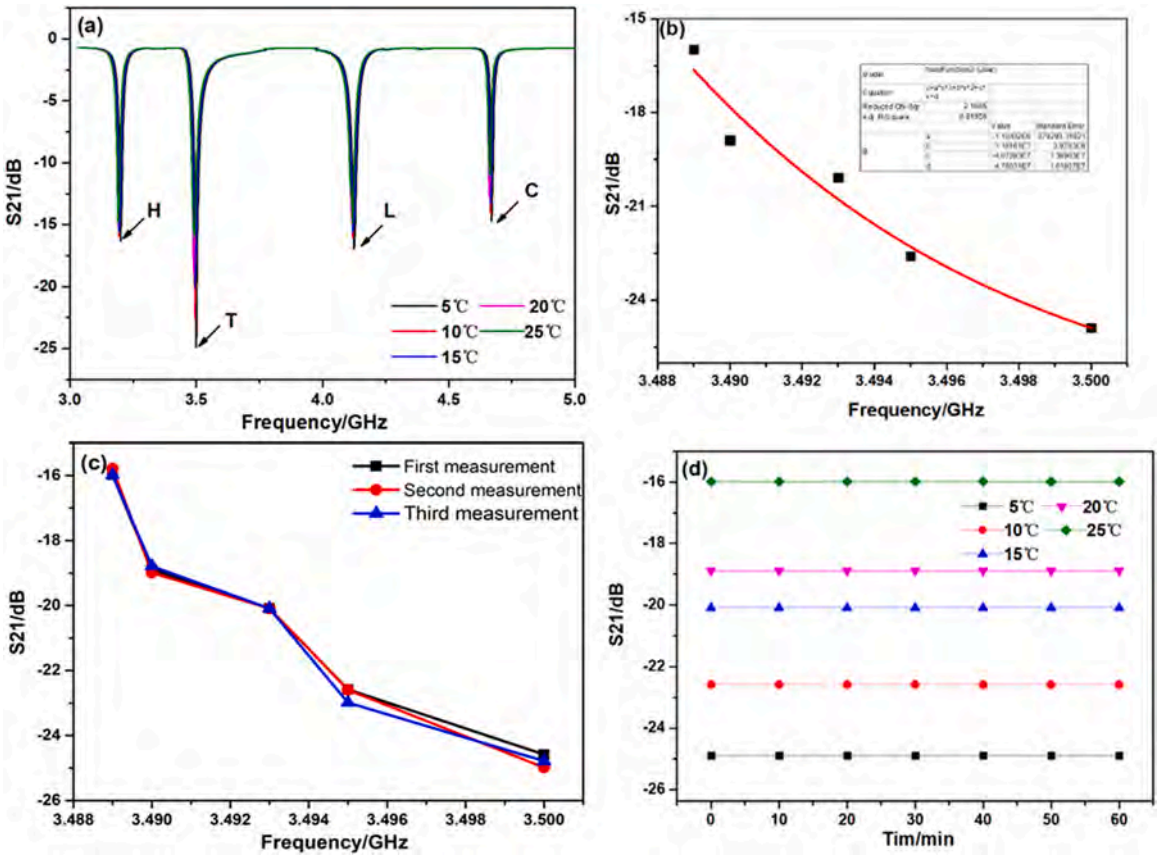

Fig. 10. (a) Effect of different temperatures on sensor f; (b) Temperature sensor f response diagram; (c) repeatability testing; (d) stability testing.

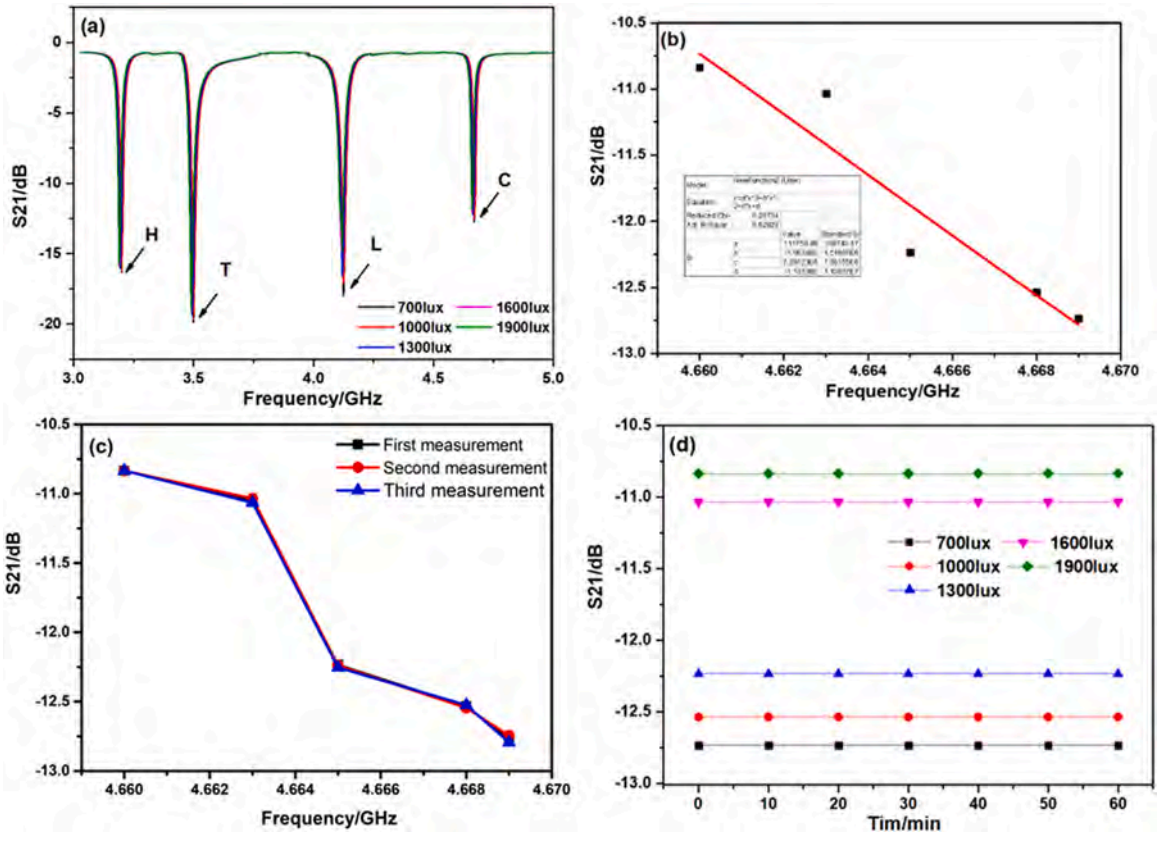

Fig. 11. (a) Effect of different light intensities on sensor f; (b) F-response diagram of the sensor; (c) repeatability testing; (d) stability testing.

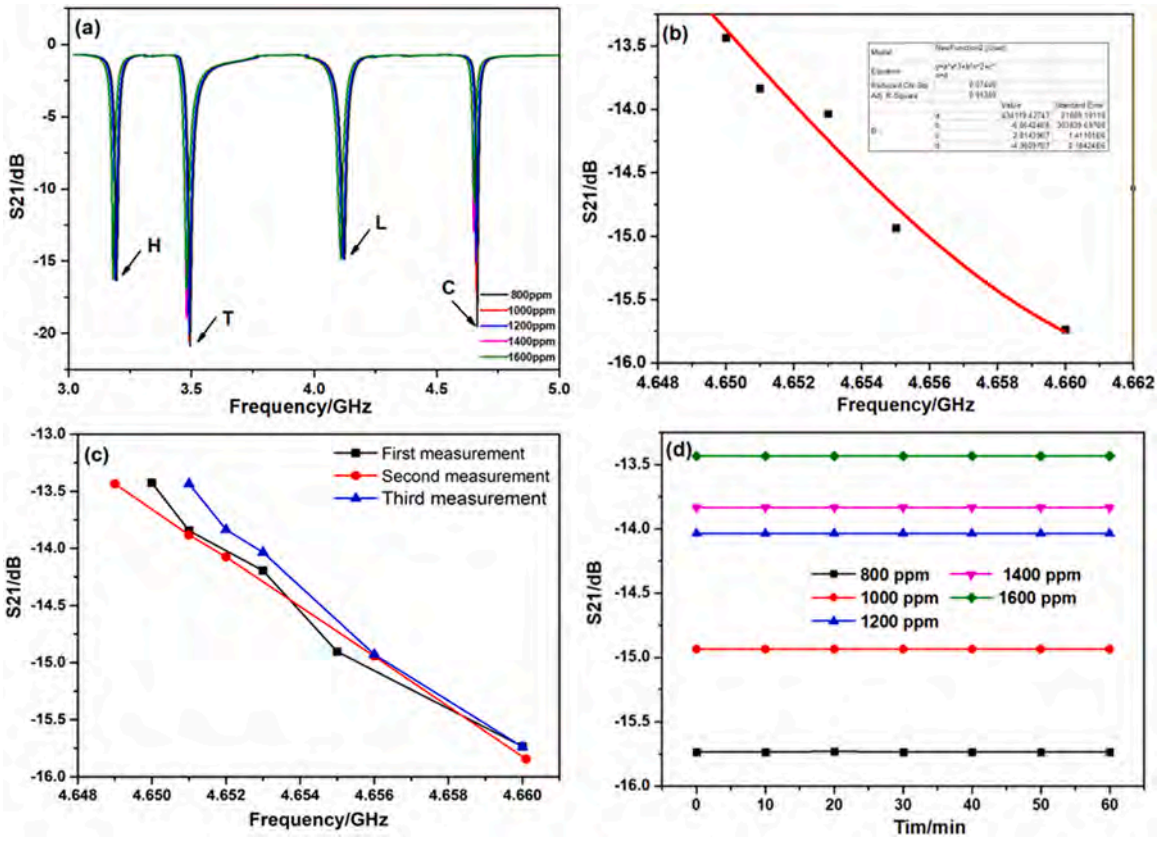

Fig. 12. (a) Effect of different CO_2 concentrations on sensor f; (b) F-response diagram of the sensor; (c) repeatability testing; (d) stability testing.

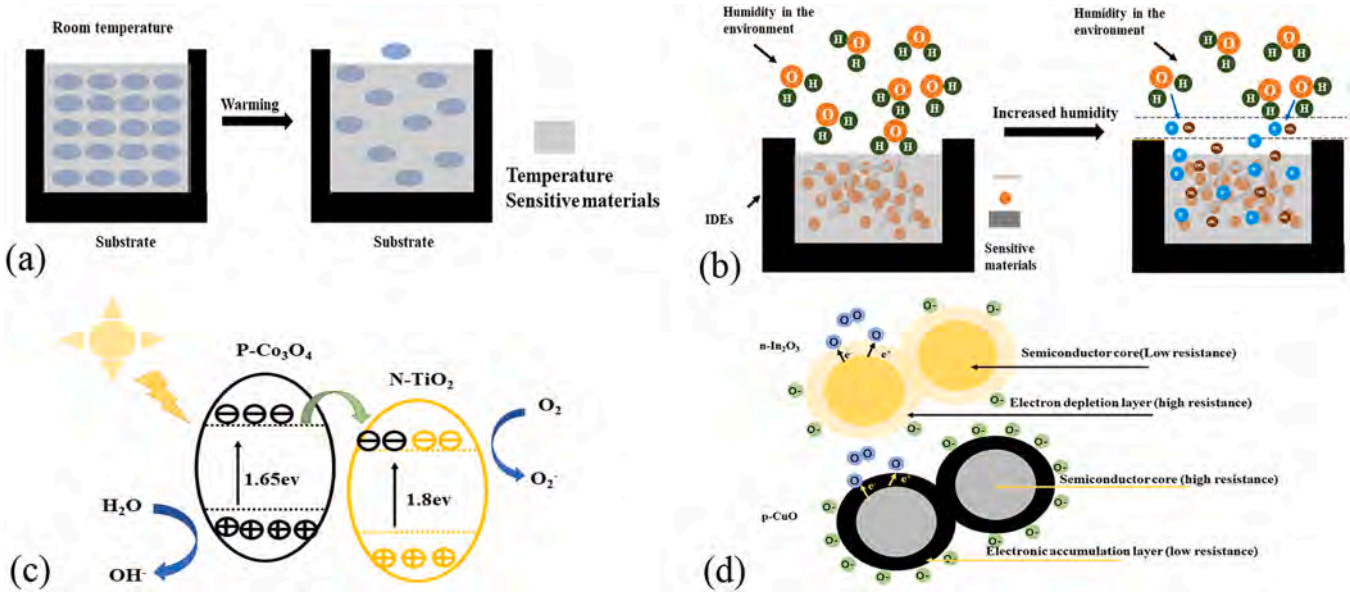

Fig. 13. (a) Humidity sensing mechanism; (b) temperature-sensitive mechanisms; (c) Light intensity sensitivity mechanisms; (d) CO_2 homicide mechanism.

dielectric constant will directly lead to changes in the antenna radiation unit. At the same time, the composite MoS2 increases the surface area of the sensitive material, and the addition of RGO increases the conductivity of the antenna sensor, making the change of dielectric constant more obvious.

As shown in Fig. 13(c) Light sensor sensitive material when the light intensity rises, the electrons in the valence band obtain the energy of the photon and jump to the conduction band, leaving free space in the valence band, the number of carriers increases, the greater the intensity of light radiation, the more electrons are excited into the empty conduction band, the number of holes increases, and the conductivity also increases with the increase of the number of carriers, causing the relative permittivity of the photosensitive material to increase, causing the amplitude of the antenna sensor to change.

As shown in Fig. 13(d), the sensitive materials sensed by CO_2 use the space charge layer model to explain the sensitive mechanism of metal

oxide gas sensitive materials and the reaction of single crystal semiconductor gas molecules, ignoring the influence of the potential barrier formed at the crystal interface on the resistance of such gas sensitive materials. Semiconductor materials for metal oxides are divided into two types: n-type and p-type. There are a large number of freely moving electrons on the conductive band of n-type metal oxide gas-sensitive semiconductor materials, and when placed in clean air, oxygen molecules in the air obtain a certain number of electrons from the conduction band, and then convert them into various forms of oxygen ions (O-, O^{2-}, O_2-), which leads to a decrease in the number of electrons inside the material and an increase in the resistance value of the material; When the n-type material is in a reducing gas, the electrons inside the gas molecules will react with oxygen ions and release the captured electrons back into the conductive band of the material, increasing the number of freely moving electrons in the conduction band and reducing the resistance value of the material; When an n-type material is placed in an oxidizing gas, the gas molecules will continue to trap electrons from the conductive band of the material, and the resistance value of the material will increase further. For p-type materials, the gas reaction process is opposite to that of n-type materials. To reduce the gas, electrons recombine with holes in the valence band, so the number of holes decreases and the resistance value of the material increases. In oxidizing gases, electrons are transferred from the valence band to gas molecules, increasing the number of holes and reducing the resistance value of the material. Causes changes in antenna parameters. In this paper, only five points of each environmental parameter are selected for measurement, and the measurement points will be added and the accuracy will be improved in subsequent experiments.

5. Conclusion

A passive RFID integrated HTLC multi-dimensional sensor is proposed, which is suitable for monitoring different environmental parameters in the agricultural growth process. In this paper, an HFSS simulation-optimized sensing antenna was prepared on the copper clad laminate by engraving machine, and nano-sensitive materials were prepared by hydrothermal method, which has the characteristics of low cost. Experimental results show that the passive RFID integrated HTLC multi-dimensional sensor works stably under conditions of 10–50 %RH, 5–25 ℃, 700–1900 Lux, 800–1600 ppm. The frequency shift of the humidity sensor is 80 MHz and the sensitivity is 2 MHz/%RH at room temperature. The amplitude change of the temperature sensor is 12.58 dB and the sensitivity is 0.63 dB/℃. The amplitude change of the light intensity sensor is 10.03 dB and the sensitivity is 0.02 dB/Lux at room temperature. The amplitude change of the CO_2 concentration sensor is 9.43 dB and the sensitivity at room temperature is 0.012 dB/ppm. Because each environmental parameter is measured by the frequency or amplitude of a separate curve, it has little influence on each other. The experimental results show that the passive RFID integrated HTLC multi-dimensional sensor can measure four environmental parameters and has large potential in environmental and agricultural monitoring.

CRediT authorship contribution statement

Fengjuan Miao: Conceptualization, Methodology, Formal analysis, Data curation, Resources, Writing - original draft, Writing - review and editing, Supervision, Project administration, Funding acquisition. **Yue Han:** Investigation, Validation, Formal analysis, Data curation, Writing - original draft. **Pengbo Tian:** Supervision, Project administration, Funding acquisition. **Bairui Tao:** Supervision, Project administration, Funding acquisition. **Yu Zang:** Supervision, Project administration, Funding acquisition. **Paul K. Chu:** Supervision, Project administration, Funding acquisition.

Declaration of Competing Interest

The authors declare that they have no known competing financial interests or personal relationships that could have appeared to influence the work reported in this paper.

Data availability

No data was used for the research described in the article.

Acknowledgements

We would like to thank the Engineering Research Center of Agricultural Multi-Dimensional Sensor Information Perception, Heilongjiang Province, and Heilongjiang Provincial Key Laboratory of Micro-Nano Sensor Component. This work was jointly supported by the Heilongjiang Higher Education Teaching Reform Project of Heilongjiang Provincial Department of Education (No. SJGY20200781), Key research and development project of Heilongjiang Province (Nos. GZ20210073, GZ20210079), Open project of Heilongjiang Key Laboratory of Micro Nano Sensors (No. WNCGQJKF202105), Fundamental Research Funds in Heilongjiang Provincial Universities (No. 145209804), City University of Hong Kong Strategic Research Grant (SRG No. 7005505), and City University of Hong Kong Donation Research Grant (DON-RMG No. 9229021).

References

[1] S. Chen, S. Brahma, J. Mackay, et al., The role of smart packaging system in food supply chain, J. Food Sci. 85 (3) (2020) 517–525.
[2] L. Motelica, D. Ficai, O.C. Oprea, et al., Smart food packaging designed by nanotechnological and drug delivery approaches, Coatings 10 (9) (2020) 806.
[3] F. Babaeian, N.C. Karmakar, Development of cross-polar orientation-insensitive chipless RFID tags, IEEE Trans. Antennas Propag. 68 (7) (2020) 5159–5170.
[4] A. Moraru, C. Ursachi, E. Helerea, A new washable UHF RFID tag: design, fabrication, and assessment, Sensors 20 (12) (2020) 3451.
[5] W. Zhu, Q. Zhang, M. Matlin, et al., Passive digital sensing method and its implementation on passive RFID temperature sensors, IEEE Sens. J. 21 (4) (2021) 4793–4800.
[6] I. Cappelli, A. Fort, M. Mugnaini, et al., Battery-less HF RFID sensor tag for soil moisture measurements, IEEE Trans. Instrum. Meas. 70 (2021) 1–13.
[7] R. Colella, M.R. Tumolo, S. Sabina, et al., Design of UHF RFID sensor-tags for the biomechanical analysis of human body movements, IEEE Sens. J. 21 (13) (2021) 14090–14098.
[8] S. Benouakta, F.D. Hutu, Y. Duroc, UHF RFID temperature sensor tag integrated into a textile yarn, Sensors 22 (3) (2022) 818.
[9] W. Zhu, Q. Zhang, M. Matlin, et al., Passive digital sensing method and its implementation on passive RFID temperature sensors, IEEE Sens. J. 21 (4) (2020) 4793–4800.
[10] N. Khalid, R. Mirzavand, H. Saghlatoon, et al., A three-port zero-power RFID sensor architecture for IoT applications, IEEE Access 8 (2020) 66888–66897.
[11] V. Mulloni, M. Donelli, Chipless RFID sensors for the Internet of Things: Challenges and opportunities, Sensors 20 (7) (2020) 2135.
[12] M. Shariq, K. Singh, A secure and lightweight RFID-enabled protocol for IoT healthcare environment: a vector space based approach, Wirel. Pers. Commun. (2022) 1–25.
[13] I. Ali, A.E.H.B. Kashyout, M. Tayel, et al., Ruthenium (Ru) doped zinc oxide nanostructure-based radio frequency identification (RFID) gas sensors for NH3 detection, J. Mater. Res. Technol. 9 (6) (2020) 15693–15704.
[14] R. Raju, G.E. Bridges, S. Bhadra, Wireless passive sensors for food quality monitoring: Improving the safety of food products, IEEE Antennas Propag. Mag. 62 (5) (2020) 76–89.
[15] Y. Zeng, X. Chen, R. Li, et al., UHF RFID indoor positioning system with phase interference model based on double tag array, IEEE Access 7 (2019) 76768–76778.
[16] S.H. Min, H.J. Kim, Y.J. Quan, et al., Stretchable chipless RFID multi-strain sensors using direct printing of aerosolised nanocomposite, Sens. Actuators A: Phys. 313 (2020), 112224.
[17] M.H. Zarifi, S. Deif, M. Daneshmand, Wireless passive RFID sensor for pipeline integrity monitoring, Sens. Actuators A: Phys. 261 (2017) 24–29.
[18] W.M. Abdulkawi, A.F.A. Sheta, Chipless RFID sensors based on multistate coupled line resonators, Sens. Actuators A: Phys. 309 (2020), 112025.
[19] Q. Li, J. Chen, L. Zhao, Research on an improved metal surface defect detection sensor based on a 3D RFID tag antenna, J. Sens. 2020 (2020) 1–13.
[20] F. Erman, E. Hanafi, E.H. Lim, et al., U-shaped inductively coupled feed UHF RFID tag antenna with DMS for metal objects, IEEE Antennas Wirel. Propag. Lett. 19 (6) (2020) 907–911.

[21] M.A.S. Tajin, W.M. Mongan, K.R. Dandekar, Passive RFID-based diaper moisture sensor, IEEE Sens. J. 21 (2) (2020) 1665–1674.
[22] F. Requena, N. Barbot, D. Kaddour, et al., Combined temperature and humidity chipless RFID sensor, IEEE Sens. J. 22 (16) (2022) 16098–16110.
[23] Y. Zhang, Q. Tan, L. Zhang, et al., A novel SAW temperature-humidity-pressure (THP) sensor based on LiNbO3 for environment monitoring, J. Phys. D: Appl. Phys. 53 (37) (2020), 375401.
[24] Q. Tan, W. Lv, Y. Ji, et al., A LC wireless passive temperature-pressure-humidity (TPH) sensor integrated on LTCC ceramic for harsh monitoring, Sens. Actuators B: Chem. 270 (2018) 433–442.
[25] W.M. Abdulkawi, A.F.A. Sheta, Four-state coupled-line resonator for chipless RFID tags application, Electronics 8 (5) (2019) 581.
[26] W.M. Abdulkawi, A.F.A. Sheta, Chipless RFID sensors based on multistate coupled line resonators, Sens. Actuators A: Phys. 309 (2020), 112025.

Fengjuan Miao received the MS degree in Power Electronics and Electrical Drives from Shanghai Maritime University, China in 2006. At July 2006 she has been teaching in Qiqihar University. Received the PhD degree at Department of Electronic Science and Technology, School of Information Science and Technology, East China Normal University , China in 2010. Her current research interests include semiconductor materials, devices, sensors and micronano electromechanical system.

Yue Han Since September 2020 he has been working towards his MS degree at Department of Electronic Science and Technology, School of Communications and Electronic Engineering , Qiqihar University. Her current research interests include semiconductor materials and sensors.

Bairui Tao received the MS degree in Electrical Engineering from East China Normal University, China in 2007. Received the PhD degree at Department of Electronic Science and Technology, School of Information Science and Technology, East China Normal University , China in 2010. His current research interests include semiconductor materials, IC design, devices and nanowire nanosensors.

Paul K. Chu received his BS in Mathematics from Ohio State in 1977 and went to graduate school at Cornell University in Ithaca, NewYork. Hewon the DuPont teaching award as a teaching assistant at Cornell in 1978 and joined the research group of Prof. George H. Morrison of the Department of Chemistry. Paul conducted research on ion beam processing and characterization of semiconductors and received his MS and PhD in Chemistry in 1979 and 1982, respectively. In 1996, he joined City University of Hong Kong as a faculty member and ventured into the new area of plasma immersion ion implantation (PIII). In 1997 he joined IEEE and he became a senior member in 1999, and he was elected Fellow of the Institute of Electrical and Electronics Engineers in 2003 for his contributions to the understanding of plasma immersion ion implantation and deposition. In 2002 he joined AVS (American Vacuum Society) and was elected Fellow of AVS in 2006 for his contributions to plasma science and surface engineering of materials and industrial components. He joined APS (American Physics Society) in 2007 andwas elected Fellowof APS in 2008 for his seminal contributions to the understanding of plasma -materials interactions aswell as development and applications of innovative plasma-based surface modification and materials synthesis technologies and instrumentation.